# Drop impact on spherical soft surfaces

Simeng Chen[1] and Volfango Bertola[1, a)]
*Laboratory of Technical Physics, School of Engineering, University of Liverpool, The Quadrangle, Brownlow Hill L69 3GH, UK*

(Dated: 24 June 2017)

The impact of water drops on spherical soft surfaces is investigated experimentally through high-speed imaging. The effect of a convex compliant surface on the dynamics of impacting drops is relevant to various applications, such as 3D ink-jet printing, where drops of fresh material impact on partially cured soft substrates with arbitrary shape. Several quantities which characterize the morphology of impacting drops are measured through image processing, including maximum & minimum spreading angle, length of the wetted curve, and dynamic contact angle. In particular, the dynamic contact angle is measured using a novel digital image processing scheme based on a goniometric mask, which does not require edge fitting. It is shown that the surface with a higher curvature enhances the retraction of the spreading drop; this effect may be due to the difference of energy dissipation induced by the curvature of the surface. In addition, the impact parameters (elastic modulus, diameter ratio & Weber number) are observed to significantly affect the dynamic contact angle during impact. A quantitative estimation of the deformation energy shows it is significantly smaller than viscous dissipation.

PACS numbers: Valid PACS appear here
Keywords: Drop impact, High-speed imaging, PDMS, Convex surface, Dynamic contact angle

## I. INTRODUCTION

Since the pioneering work of Worthington[1], the collision of drops with solid surfaces has attracted the interests of many researchers for decades[2–6]. Various post-impingement behaviours of droplets have been characterized systematically, including spreading, receding, splashing & bouncing *etc.* Most of the existing research concerns the simple scenario in which drops impact on rigid flat surfaces. However the role of the compliance of soft substrates is important to understand since it is involved in various application such as the delivery of pesticides on leaves[7] and the spray cooling of flexible surfaces. Also it is suggested that the use of a compliant coating on some materials could reduce the damage of erosion processes caused by drop impacts[8]. The majority of the early research works on the role of the substrate compliance in drop impact considers a solid elastic surface. It has been shown that the surface tension component of the drop liquid perpendicular to the surface of elastic substrate can significantly influence the wetting behaviours at the three-phase contact line (TPCL)[9–13]. This is to due to the formation of a 'wetting ridge', with length scales ranging from tens of nanometers to several micrometers. A more recent study reports that the formation of 'wetting ridge' associated with the viscoelastic nature of the substrate is able to slow the motion of the TPCL, which is referred as the 'visoelastic braking' effect[14]. A systematic experimental investigation of the drop impact on soft PDMS substrates was carried out by Mangili *et al.*[15], who found the recoil phase on soft substrates is slower when compared to drop impacts on hard substrates and significant deformation (on the order of tens of micrometer) of soft substrates was observed during impact. The fact that the retraction of impacting drops decreases with decreasing substrate elasticity is confirmed by the work of Alizadeh *et al.*[16], however in this study it is also shown that the substrate elasticity has very little effect on the dynamics of impacting drops on textured surfaces with periodic arrays of microstructures (superhydrophobic surfaces). In another experimental study of drop impact on soft PDMS surfaces[17], the evolution of the entrapped air under an impact droplet is investigated. A thin air film during the impact is observed due to the shear-thinning property of the surface, which reduces the surface energy and leads to the rebound of the droplet. The substrate stiffness is shown to affect the splashing threshold[18,19]. Compared to rigid substrate, splashing is reduced or even eliminated due to the absorption of the kinetic energy of the impacting drop by the deformation of the substrate. The substrate flexibility is also found to enhance the superhydrophobicity of the surface[20,21], resulting in less contact time for the rebound of the impacting drop. Besides the investigations on solid elastic surfaces, Gart *et al.* consider a cantilever system[22], where it is found that the hydrophobicity of the surface can reduce the torque experienced by the bending beam. While most of the existing literature has a focus on PDMS or other hydrophobic substrates, some is limited to an elastic or viscoelastic surface, there are some interesting experiments on wetting on soft hydrophilic substrates[23]. Recently, the study of drop impact on soft surfaces has been extended to a viscoplastic system[24], where the impact morphology of different drop/substrate combinations of yield stress values is studied experimentally. The permanent nestling of the drop fluid in the substrate under the impact point is

a)Electronic mail: Volfango.Bertola@liverpool.ac.uk

observed and the final profile is strongly affected by the yield stress magnitudes of the drop and of the substrate.

The geometrical shapes of target surfaces may not always be planar in many industrial applications. For example, drop impact on curved surfaces of cylinders in horizontal-tube falling film evaporators, in the manufacturing of digital displays consisting of numerous polymer light-emitting diodes, or drops of polymer liquid impact on rectangular microcavities[25]. Thus, a better understanding of the effect of arbitrary shape of the surface on the dynamics of impacting drops is necessary. Hardalupas *et al.* conduct experiments on sub-millimetre droplet impingement onto spherical surfaces with diameters of the order of 1 mm, and it was found that the onset of reatomisation is promoted with the increase of surface curvature[26]. Motivated by the aim to measure the spatial and temporal variation of film thickness during drop impact, which is extremely difficult for drop impact on a flat surface, Bakshi *et al.*[27] investigate the impact of a droplet onto a spherical target experimentally and theoretically. Reynolds number and target-to-drop size ratio are observed to affect the dynamics of the film flow on the surface of the target. Additionally, an experimental study on the drop impact of heptane and butanol on wetted spheres shows that the spreading factor defined as the ratio between the spreading area and the drop surface area increases as the curvature ratio grows or liquid viscosity reduces[28].More recently the dynamics of drop impact on spherical surfaces has been simulated numerically using different methods including Lattice-Boltzmann method and Volume of Fluid method[29–31], results show good agreement with the existing experimental data in literatures. Besides a spherical shape of the impact surface, the drop impact on substrates of other arbitrary shapes has also been investigated experimentally and numerically, such as cylindrical surfaces[32–34] or rectangular microcavities[25,35].

The objective of this research is to investigate the combined effect of substrate compliance (*i.e.* elasticity) and curvature (*i.e.* diameter ratio between hemispherical substrate and equilibrium drop) on the morphology of the impacting drops at different Weber numbers. The effect of a convex compliant surface on the dynamics of impacting drops is important to understand since it is involved in various applications. For instance, in 3D ink-jet printing, drops of fresh material impact on a half-cured soft substrate with arbitrary shape. In particular, the spreading and retracting behaviours are characterized in this study. A novel image-processing technique based on a goniometric mask is adopted to measure the dynamic contact angle during the impact process[36–38]. In conventional goniometry methods, contact angles are generally measured by fitting one or more analytical functions to the drop shape (*e.g.* the Axisymmetric Drop Analysis method)[39–41]. Compared to these methods, the novel technique does not require either the drop symmetry or the drop shape of a spherical cap, which is desirable when measuring the dynamic contact angle of drop impact on convex surfaces.

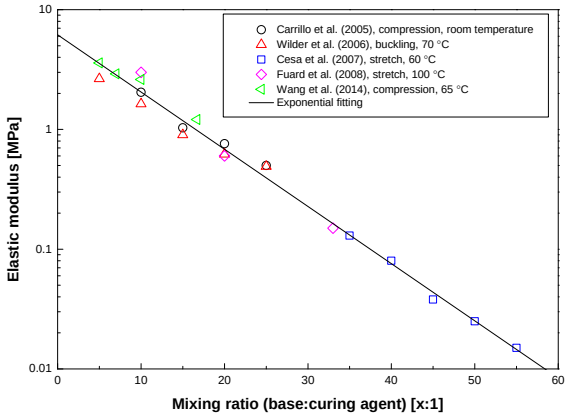


FIG. 1: The measured elastic modulus of PDMS as a function of mixing ratio reported by different research groups.

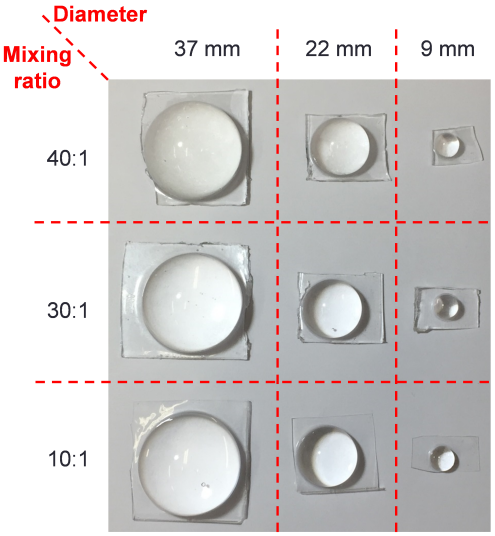


FIG. 2: Manufactured samples of hemispherical PDMS substrates of different diameters and mixing ratios.

## II. EXPERIMENTAL SETUP AND METHOD

### A. Convex hemispherical elastic substrates

The convex hemisphere elastic substrates were manufactured using polydimethylsiloxane (PDMS). The commercial product Sylgard 184 (SigmaAldrich) was selected since it has been widely used in previous works. The elastic modulus of PDMS can be adjusted by changing the mixing ratio of the base polymer and the crosslinker. Figure 1 shows the measured experimental data of the elastic moduli of PDMS as a function of the mixing ratio reported by five research groups[42–46]. The methods for

TABLE I: Elastic modulus of PDMS of different mixing ratios.

| Mixing ratio | 10:1 | 30:1 | 40:1 |
|---|---|---|---|
| Elastic modulus (MPa) | 2.05 | 0.23 | 0.08 |

measurement include compression, stretch and buckling. The baking temperatures range from room temperature to 100 °C. It is observed that the experimental data obtained by different researchers show very good consistency and the elastic modulus decreases exponentially as the mixing ratio grows. Thus all the data are fitted into an exponential model, which yields a coefficient of determination $R^2 = 0.988$:

$$\mathrm{E} = 6.17 \cdot e^{-0.11\mathrm{x}}, \quad (1)$$

where x represents the mixing ratio of the base and the curing agent. In order to study the effect of the elastic modulus on the impact morphology of the drop, three different mixing ratios are selected to manufacture the substrates: 10:1, 30:1 & 40:1. The corresponding elastic moduli of the PDMS of different mixing ratios are calculated using Equation 1 and the values are shown in Table I.

PDMS hemispheres of different diameter were produced by curing the Sylgard 184 compound in a suitable mould. After the mould was filled with the mixture of base and curing agent, it was baked in an oven at 65 °C for 24 hours to make sure the sample was completely cured[45]. Some manufactured samples of hemispherical PDMS substrates of different diameters and mixing ratios are displayed in Figure 2.

It has been experimentally shown that the contact angle hysteresis ($\Delta\theta = \theta_{\mathrm{ad}} - \theta_{\mathrm{re}}$, where $\theta_{\mathrm{ad}}$ represents the advancing contact angle and $\theta_{\mathrm{re}}$ the receding contact angle) changes with the elastic modulus of the soft substrates[9]. The static contact angle and contact angle hysteresis of water drop on flat PDMS substrates with the same elastic moduli as the hemispherical substrates used in the present experiments were measured, and their values are reported in Table II. Advancing and receding contact angles were measured using the volume change method; the advancing contact angle was measured by recording the gradually growing droplet (increasing volume) through the injection of liquid from a needle, whereas the receding contact angle was measured by decreasing the volume. As shown in Table II, the contact angle hysteresis increases significantly as the elastic modulus decreases. Especially in the case of the softest surface (E=0.08 MPa), the decrease in the drop volume does not lead to retraction of the contact line and the liquid periphery remains pinned until the volume reduces to zero; thus, in this case the receding contact angle is almost zero. The experimental data in Table II is consistent with the data reported in a previous experimental investigation[15].

TABLE II: Static, advancing & receding contact angle ($\theta_0$, $\theta_{\mathrm{ad}}$ & $\theta_{\mathrm{re}}$) and contact angle hysteresis ($\Delta\theta$) of flat substrates with the same elastic moduli in experiments

| E [MPa] | $\theta_0$ [°] | $\theta_{\mathrm{ad}}$ [°] | $\theta_{\mathrm{re}}$ [°] | $\Delta\theta$ [°] |
|---|---|---|---|---|
| 2.05 | $104 \pm 3$ | $118 \pm 2$ | $81 \pm 3$ | $38 \pm 5$ |
| 0.23 | $115 \pm 6$ | $123 \pm 5$ | $49 \pm 4$ | $73 \pm 5$ |
| 0.08 | $114 \pm 2$ | $128 \pm 3$ | 0 | $128 \pm 3$ |

TABLE III: Values of the impact parameters.

| Elastic modulus $E$ [MPa] | Diameter ratio $D^*$ [-] | Weber number $We$ [-] |
|---|---|---|
| | | 14 |
| 2.05 | 2.91 | 47 |
| 0.23 | 7.12 | 81 |
| 0.08 | 12.0 | 114 |
| | | 147 |

### B. Experimental setup

The experimental setup is conceptually similar to those used in previous drop impact studies[47,48]. Drops of deionized water (Barnstead Easypure, $\rho = 1 \times 10^3$ kg/m$^3$ & $\sigma = 72.75$ mN/m) are released from a blunt hypodermic needle (gauge 21, i.d. 0.495 mm) and impact on the centre ("north pole") of the hemispherical PDMS substrate. Drop weight measurements made with a precision balance (Denver Instrument TP-124A) allow calculation of the drop diameter at equilibrium: $D_0 = \sqrt[3]{(6m/\pi\rho)}$, where $m$ denotes the average drop mass. Value of equilibrium drop diameter is obtained from averages over 50 samples, which yields $D_0 = 3.09 \pm 0.09$ mm. Adjusting the position of the dispensing needle with a digital height gauge allows one to change the impact velocity hence the impact Weber number, $We = \rho D_0 u_i^2/\sigma$, which expresses the competition between kinetic energy and surface energy. The impact velocities $u_i$ are measured through digital image processing.

In this study, each set of experimental parameters contains three variables: (a), the elastic modulus of the substrate; (b), the diameter ratio, which is defined as the ratio of the hemispherical substrate diameter ($D_{sub}$) to the drop equilibrium diameter $D^* = D_{sub}/D_0$; (c), the impact Weber number. Values of the impact parameters are presented in Table III. For each set of experimental parameters (i.e., elastic modulus, diameter ratio and Weber number), the impact experiment is repeated five times for the sake of statistical analysis.

The impacts of single drops are recorded using a high-speed CMOS camera (Mikrotron MC1310) with a resolution of $640 \times 365$ pixels at the rate of 2000 frames per second. Magnification was kept constant throughout all experiments and lengths on the image could be calculated by comparison with the reference length of the substrate diameter (spatial resolution: 21 $\mu$m/pixel). The camera

is horizontally aligned with the impact surface in order to measure the bouncing height of the drop with precision. Back-to-front illumination is provided by an LED lamp (Philips Accent LED), which ensures a uniform intensity in the field of view.

### C. Image processing

The recorded images by high-speed camera were processed through a self-developed Matlab program, which allows one to observe the contour of the deforming drop and obtain quantitative measurements. Figure 3 shows an example of how the recorded grayscale image (I) is converted to the processed RGB image (I*). Image I represents a snapshot which is taken 6 ms after impact at Weber number 47, elastic modulus 2.05 MPa & diameter ratio 2.91. The whole process consists of two steps. In the first step, both the image during impact (I, drop & substrate) and the image before impact (S, substrate) are converted into binary images through image thresholding. Then the contour of the deforming drop ($D_b$) is obtained by subtracting the hemispherical substrate ($S_b$) from the binary image containing both the drop and the substrate ($I_b$). In the second step, the binary images of the substrate and the drop ($S_b$ & $D_b$) are coloured into RGB images ($S_c$ & $D_c$). In order to differentiate between the substrate and the drop, they are coloured red and blue respectively. Finally the RGB image of the drop is superimposed on the RGB image of the substrate, which produces the processed RGB image (I*).

A schematic of the contact angle measurement procedure is shown in Figure 4. Firstly the centre of the hemispherical substrate must be found before any further measurements can be done. This is achieved by solving the coordinates of the centre using the coordinates of three randomly selected points (e.g. $P_1$, $P_2$ & $P_3$) on the arc of the substrate since three noncollinear points determine a circle. Secondly the left & right contact points, $C_L$ & $C_R$, are identified and the value of the angle $\angle C_L O C_R$ (referred as the 'base angle', $\alpha = \theta_L + \theta_R$) is measured.

The dynamic contact angle measurement is achieved by goniometric-mask method[36,38]. However this method is only able to measure the angle with respect to the horizontal line (e.g. $\theta_{Rx}$ & $\theta_{Lx}$ in Figure 4) from the digital image. By means of some simple geometrical analysis, the actual dynamic contact angles can be calculated as follows:

$$\theta_{RC} = \theta_{Rx} - \theta_R \ (\theta_{LC} = \theta_{Lx} - \theta_L), \tag{2}$$

where $\theta_{RC}$ (or $\theta_{LC}$) represents the dynaminc contact angle on the right (or left) side of the view, and $\theta_{Rx}$ (or $\theta_{Lx}$) denotes the measured angle of the tangential line of the drop contour at the contact point with respect to $x$-axis, and $\theta_R$ (or $\theta_L$) is the angle between line $\overline{OC}_R$ (or $\overline{OC}_L$) and $y$-axis.

### D. Quantitative measurements

The contact angle measurement via the goniometric mask method depends on the mask size[36,38]. The mask size, z, strongly affects the angle measurement because a discrete mask can resolve a maximum number of discrete angle values equal to the number of pixels in the triangle, $(z+1)^2/4$. Thus, the minimum value (in radians) that can be measured, corresponding to one pixel, is $4/(z+1)^2$; for example, to measure an angle of 1°, the mask size should be $z = \sqrt{180} - 1 = 25$. Thus, a mask size of 25x25 pixels is the minimum size to achieve a resolution of 1. The algorithm performance is a trade-off between the mask size and the mask size/image size ratio; on one hand, increasing the mask size pays back in terms of accuracy but, on the other hand, if the image size to mask size ratio is too small angles are not measurable. In other words, the optimal mask size is a trade-off between the need to capture the drop contour curvature near the contact point, which requires a smaller mask, and the need to obtain more accurate measurement, which requires a larger mask. For this reason, the measurements of the dynamic contact angles are taken in a range of mask size from 1 to 81 pixels with the following impact parameters: $We = 14$, $E = 2.05$ MPa & $D^* = 2.91$. In particular, two snapshots after impact are selected as shown in Figure 5: (a), t = 5.5 ms (in spreading phase); (b), t = 15.5 ms (in retracting phase). In case (a) the measured contact angles on both left and right sides ($\theta_{OL}$ & $\theta_{OR}$) are obtuse, while in case (b) two acute angles are measured ($\theta_{AL}$ & $\theta_{AR}$). The measured results of four contact angles as a function of mask size $z$ are shown in Figure 6. The mask size was set to 25 pixels for all the contact angle measurements in this study. In order to further validate the measurement method, the temporal variation of left dynamic contact angle in the same case is measured at $z$=25 pixels as shown in Figure 7. The results are compared with the results of a smaller mask size $z$=19 pixels and a bigger mask size $z$=31 pixels. The high consistency among the results implies that the measurement method is valid and the choice of mask size is reasonable.

Another obvious quantity of interest is the substrate deformation caused by drop impact. In the case of a flat substrate, the substrate deformation can be calculated by inserting a cantilever into the PDMS substrate just under the impact point, and measuring the displacement of the free end of the cantilever[15]. Unfortunately, in the case of spherical substrate this method cannot be used, because due to the substrate curvature the impact surface is not parallel to the cantilever, and the cantilever would be moved by the expanding drop, which causes a displacement of the free end at least one order of magnitude larger than the displacement caused by the PDMS deformation only. According to the experimental results by Mangili et al.[15], in case of a flat PDMS substrate with an elastic modulus of 0.017 MPa an impacting drop with vertical velocity of about 2m/s (We ≈ 152) will cause a maximum substrate deformation of ≈ 40 $\mu$m. In the present work,

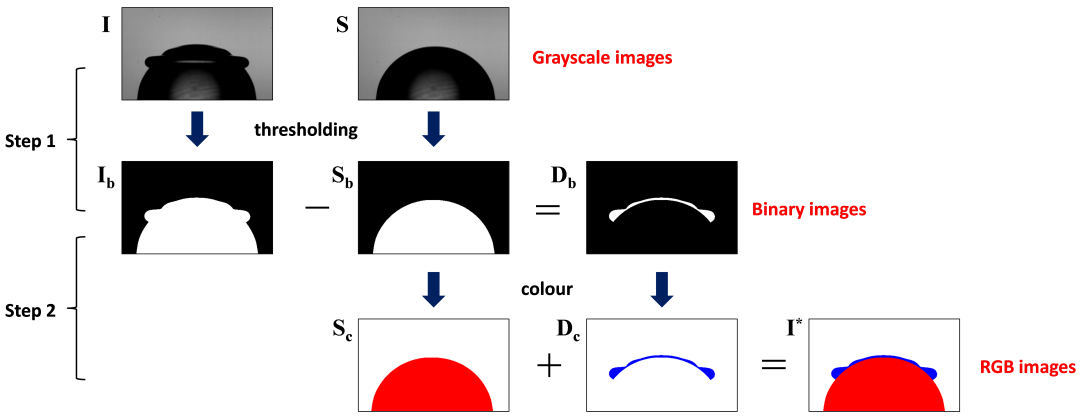


FIG. 3: Schematic of the image processing.

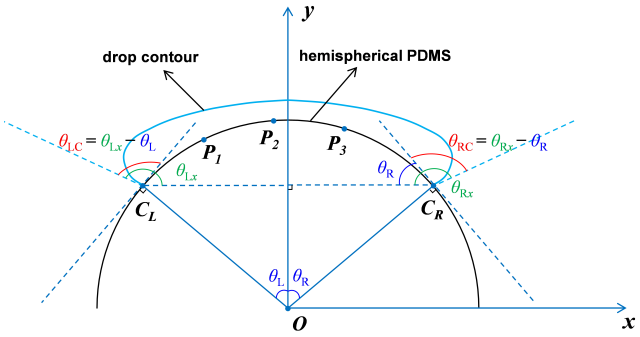


FIG. 4: Schematic of the contact angle measurement procedure.

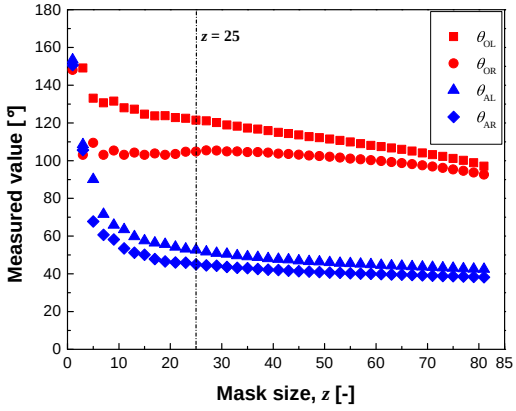


FIG. 6: Measured contact angles as a function of mask size.

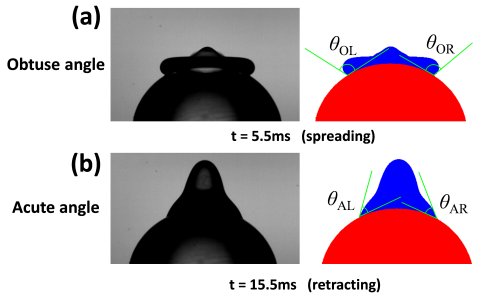


FIG. 5: Contact angles at different stages: (a) spreading, (b) retracting.

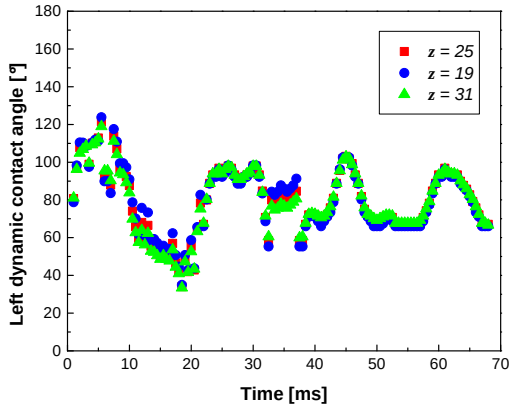


FIG. 7: Measured dynamic contact angles (left) as a function of time after impact.

the maximum Weber number is 147 and the lowest elastic modulus is 0.08 MPa (i.e., almost five times larger than 0.017 MPa), hence one can estimate a maximum deformation of the order of 8-9$\mu$m, which is below the spatial resolution of these measurements (21$\mu$m/pixel).

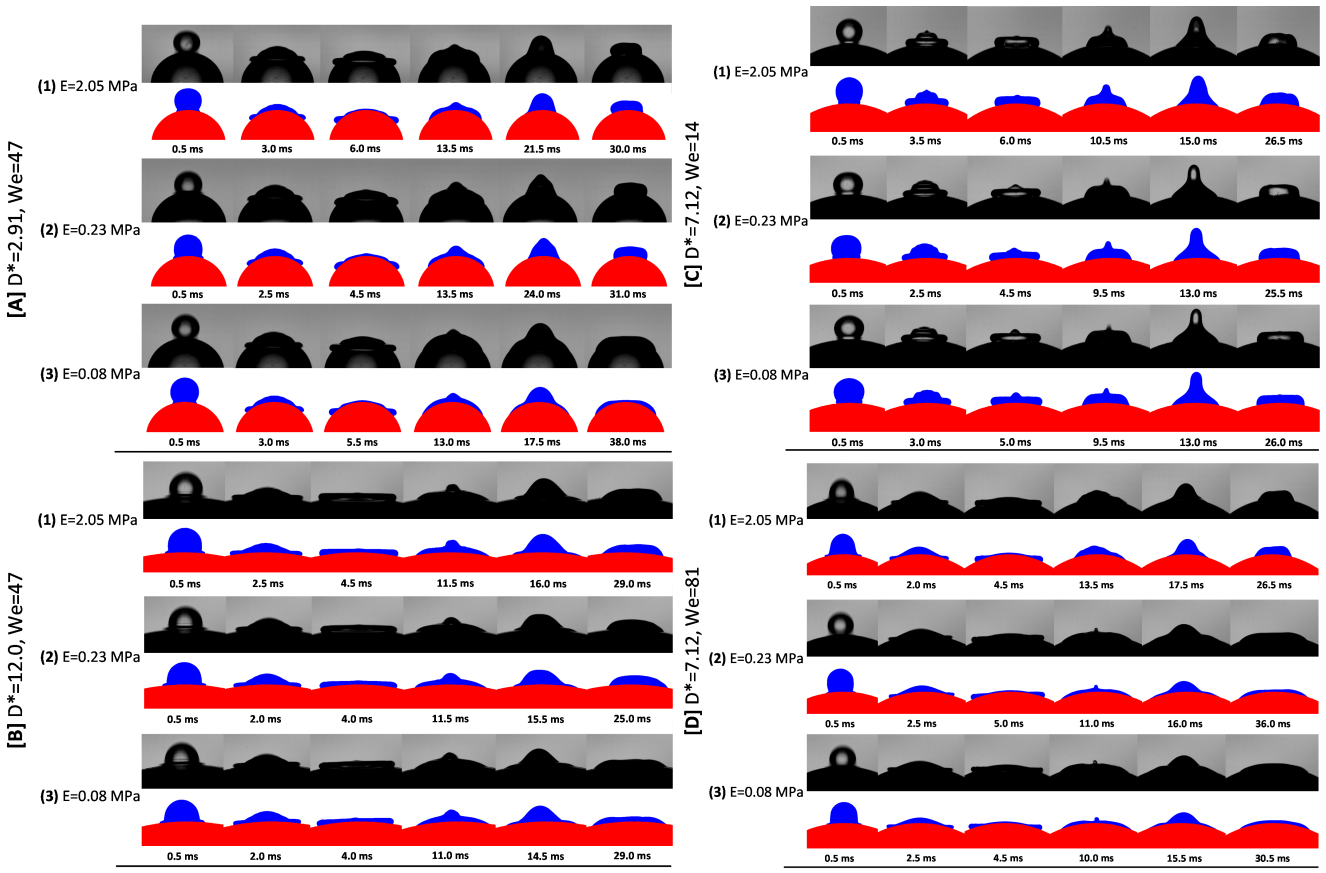


FIG. 8: Morphology of drop impact on elastic convex surfaces showing the effect of **elastic modulus**. For each group (**A**, **B**, **C** & **D**) of image sequences the elastic modulus decreases from **(1)** to **(3)**: **(1)** E = 2.05 MPa, **(2)** E = 0.23 MPa & **(3)** E = 0.08 MPa. In order to show the effect of E under various conditions, different combinations of the other two impact parameters ($D^*$ & We) are chosen for each group: **A**, $D^*$ = 2.91, We = 47; **B**, $D^*$ = 12.0, We = 47; **C**, $D^*$ = 7.12, We = 14; **D**, $D^*$ = 7.12, We = 81. The first row in each case represents the recorded images and the second row shows the processed images.

## III. EXPERIMENTAL RESULTS

### A. Morphology

#### 1. Effect of elastic modulus on morphology

The morphology of drop impact on elastic convex surfaces showing the effect of elastic modulus is displayed in Figure 8. In particular, four groups of image sequence are selected: Group A & Group B compare the results at the same Weber number but different diameter ratios while Group C & Group D compare the results at the same diameter ratio but different Weber numbers. The impact morphologies of the two cases of high elastic moduli in Group A (A(1) & A(2)) are almost the same: the drop firstly spreads on the convex surface until the spreading angle reaches its maximum and then the thin liquid cap starts to recoil as the contact angle decreases. A central column of liquid may be observed at the end of the retraction stage (as shown by the last but one image). After the initial retraction the drop sits on the top of the hemisphere and oscillate periodically between horizontal direction and vertical direction. This stage is dominated by capillary forces. But for the case of low elastic modulus (A(3)), the liquid cap fails to retract and the rim of the liquid is almost pinned at the maximum spreading location. The height of central liquid column is also smaller than other two cases due to this pinning effect. However in the case of a higher impact Weber number ($We$ = 81) and a greater diameter ratio ($D^*$ = 7.12) as shown in Group C, besides the substrate with the lowest elastic modulus, the substrate with the intermediate elastic modulus (D(2)) also exhibits the 'pinned effect'. This effect becomes less pronounced at a relatively low impact Weber number and high diameter ratio (e.g. see Group B & C). Generally the spreading phase is not affected greatly by the elastic modulus. No splashing or breakup was observed in the range of Weber numbers considered, in agreement with other studied that demonstrated a strong increase of the splashing threshold due

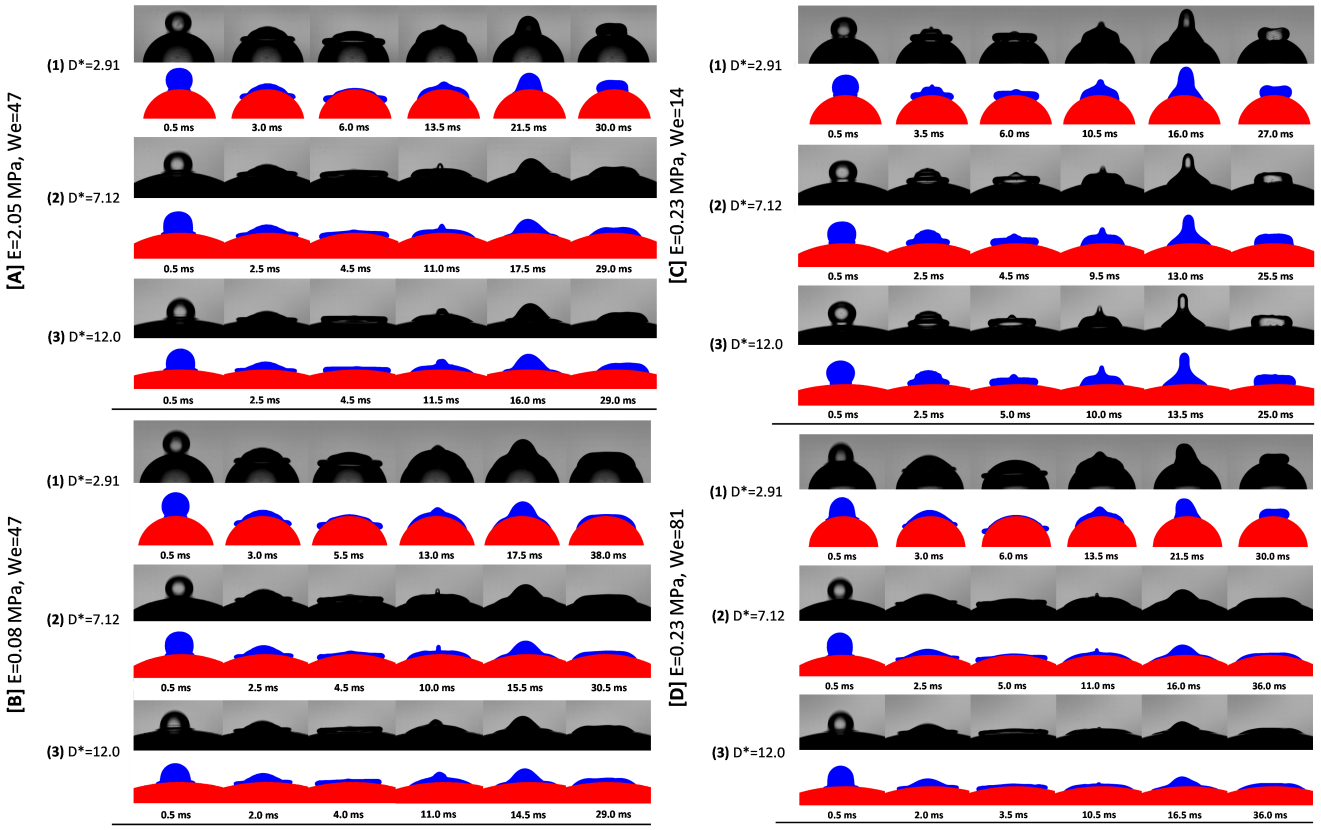


FIG. 9: Morphology of drop impact on elastic convex surfaces showing the effect of **diameter ratio**. For each group (**A**, **B**, **C** & **D**) of image sequences the diameter ratio increases from **(1)** to **(3)**: **(1)** $D^*$ = 2.91, **(2)** $D^*$ = 7.12 & **(3)** $D^*$ = 12.0. In order to show the effect of $D^*$ under various conditions, different combinations of the other two impact parameters (E & We) are chosen for each group: **A**, E = 2.05 MPa, We = 47; **B**, E = 0.08 MPa, We = 47; **C**, E = 0.23 MPa, We = 14; **D**, E = 0.23 MPa, We = 81. The first row in each case represents the recorded images and the second row shows the processed images.

to the absorption of the kinetic energy of the impacting drop by the deformation of the substrate[18,19].

### 2. Effect of diameter ratio on morphology

Figure 9 shows the effect of diameter ratio on the morphology of drop impact on elastic convex surfaces. Specifically four groups of image sequence are selected: Group A & Group B compare the results at the same Weber number but different elastic moduli while Group C & Group D compare the results at the same elastic modulus but different Weber numbers. In Group A, surprisingly the case with the smallest diameter ratio (A(1)) exhibits the largest degree of retraction even though the gravity component applied on the liquid rim along the tangential direction is higher during both spreading and retracting phases than the other two cases. And the height of the liquid column formed after recoiling is greater compared to large diameter ratio cases. This effect has also been observed in Group D. Here it is proposed that this 'de-wetting effect' is due to the combinational influence of gravity and large curvature of the impact surface, which leads to a large dynamic contact angle at the beginning of retraction. For cases with very low elastic modulus, where the 'pinned effect' dominates, and very low impact Weber number (e.g. Group B & C) the 'de-wetting effect' becomes less significant.

### 3. Effect of Weber number on morphology

The effect of the impact Weber number on the impact morphology is displayed in Figure 10. Four groups of image sequences are selected: Group A & Group B compare the results at the same diameter ratio but different elastic moduli, while Group C & Group D compare the results at the same elastic modulus but different diameter ratios. As the impact Weber number increases, due to the curvature of the surface, the central part of the liquid lamella is no longer covered by the rim and becomes visible (e.g. Group A, B & D). Moreover flow instabilities are observed at high impact Weber number during the spreading stage as indicated by the wavy shape near

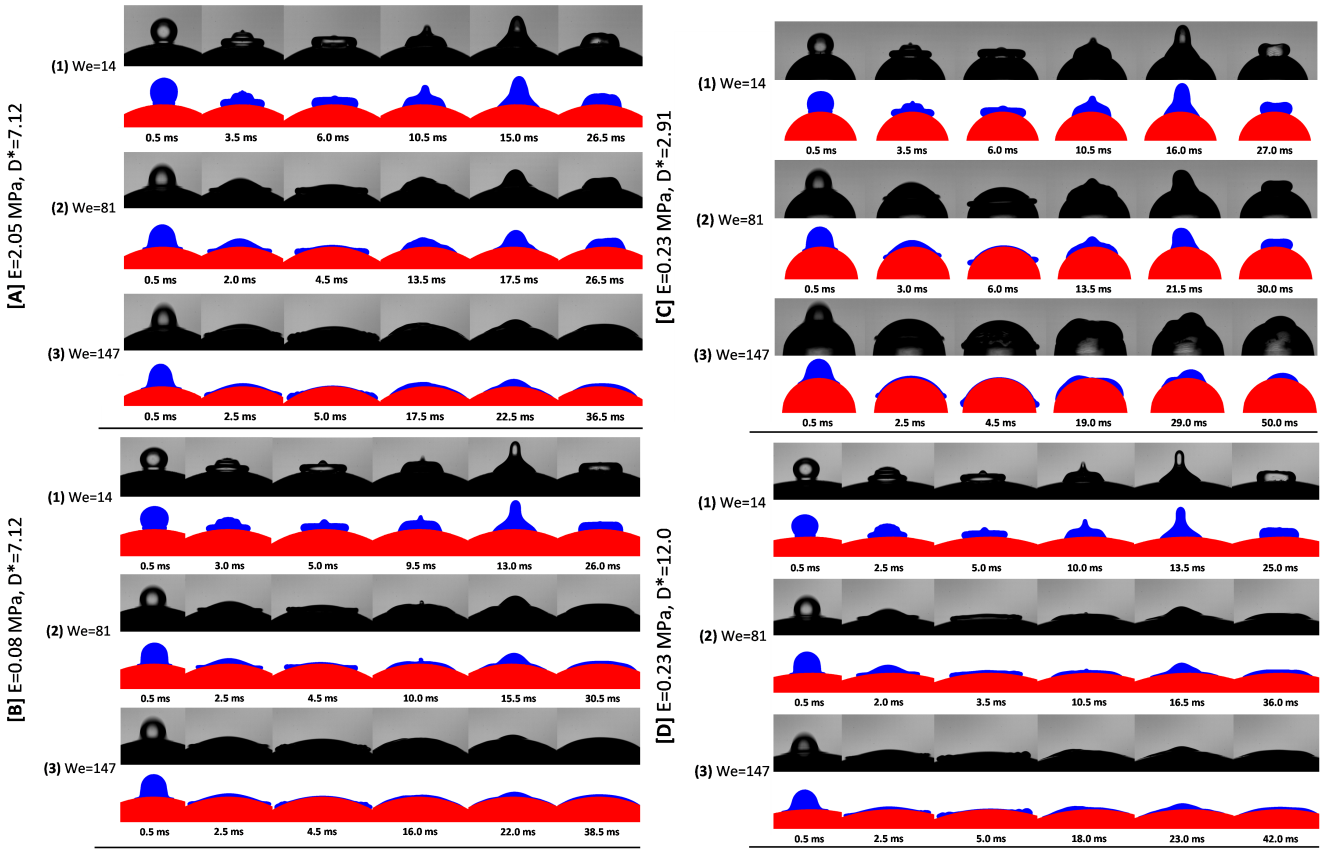


FIG. 10: Morphology of drop impact on elastic convex surfaces showing the effect of **impact Weber number**. For each group (**A**, **B**, **C** & **D**) of image sequences the Weber number increases from **(1)** to **(3)**: **(1)** We = 14, **(2)** We = 81 & **(3)** We = 147. In order to show the effect of $D^*$ under various conditions, different combinations of the other two impact parameters (E & $D^*$) are chosen for each group: **A**, E = 2.05 MPa, $D^*$ = 7.12; **B**, E = 0.08 MPa, $D^*$ = 7.12; **C**, E = 0.23 MPa, $D^*$ = 2.91; **D**, E = 0.23 MPa, $D^*$ = 12.0. The first row in each case represents the recorded images and the second row shows the processed images.

the rim of the spreading lamella in (3) for all groups. In case C(3), the flow instabilities cause symmetry breaking during the retraction. As a result the drop partially slide off the top of the hemisphere.

### B. Maximum spreading & minimum retracting

After impact the drop spreads radially from the top of the hemisphere to form a cap, and the base angle attains its maximum value at the end of the spreading stage. The maximum spreading angle ($\alpha_{\max}$) for different impact parameters is measured through digital image processing. If the same liquid lamella (i.e. the same surface energy) is deposited on hemispheres with different diameters, obviously the hemisphere with the lowest diameter will give the largest spreading angle. Thus the maximum spreading angle is very dependent of $D^*$ and it is more reasonable to plot the normalised maximum length of the wetted arc (denoted by $\widehat{C_L C_R}$ in Figure 4): $L_{\max} = (\alpha_{\max}/180°) \cdot \pi \cdot (D_{sub}/2)$, which is proportional to the surface energy of the liquid cap, as a function of the Weber number for different impact parameters as shown in Figure 11. Data with the same diameter ratio are marked using the same colour (red: $D^*$ = 2.91, green: $D^*$ = 7.12 & blue: $D^*$ = 12.0). Good consistency is exhibited by the experimental data in the considered Weber number range, where follow a scaling law[49] ($L_{\max}/D_0 \sim \mathrm{We}^{0.33}$) indicated by the solid line, which implies that the spreading behaviours are still dominated by the Weber number (*i.e.* the effect of elastic modulus and diameter ratio is negligible).

After maximum spreading, the drop recoils to the top of the hemisphere and starts to oscillate. The minimum base angle reached at the end of the initial retraction phase is referred to as the 'minimum retracting angle' ($\alpha_{\min}$). The normalised minimum length of the wetted arc (defined the same way as $L_{\max}$ but with $\alpha_{\min}$) as a function of impact Weber number for different impact parameters is plotted in Figure 12. Unlike the spreading behaviour, the retracting behaviour is strongly affected by the magnitude of the elastic modulus of the substrate.

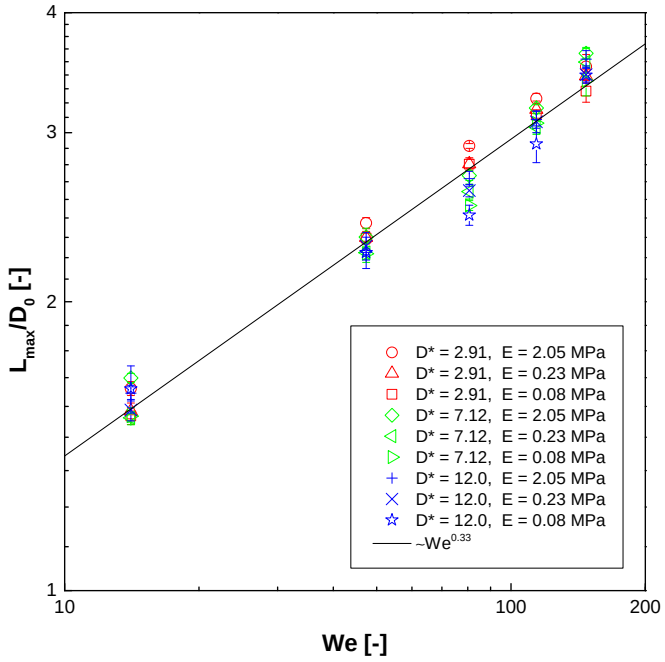


FIG. 11: Maximum length of the wetted arc (normalized by equilibrium drop diameter) as a function of impact Weber number for cases of different diameter ratios and elastic moduli.

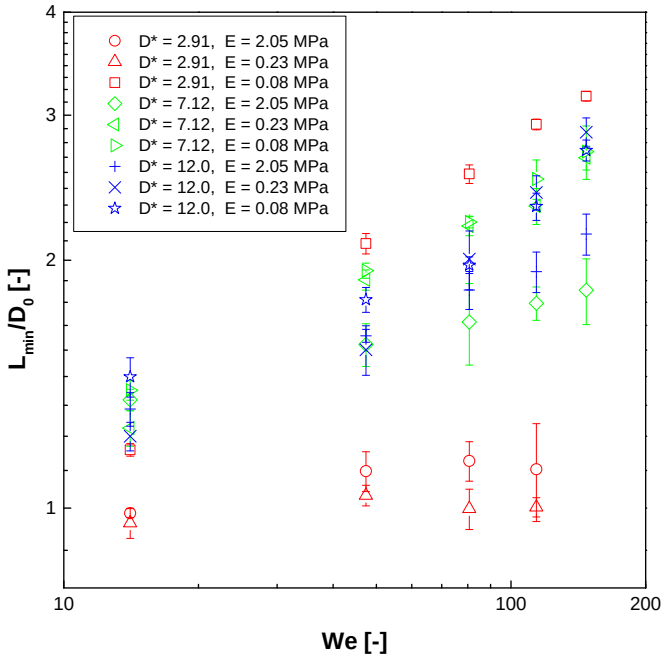


FIG. 12: Minimum length of the wetted arc (normalized by equilibrium drop diameter) as a function of impact Weber number for cases of different diameter ratios and elastic moduli.

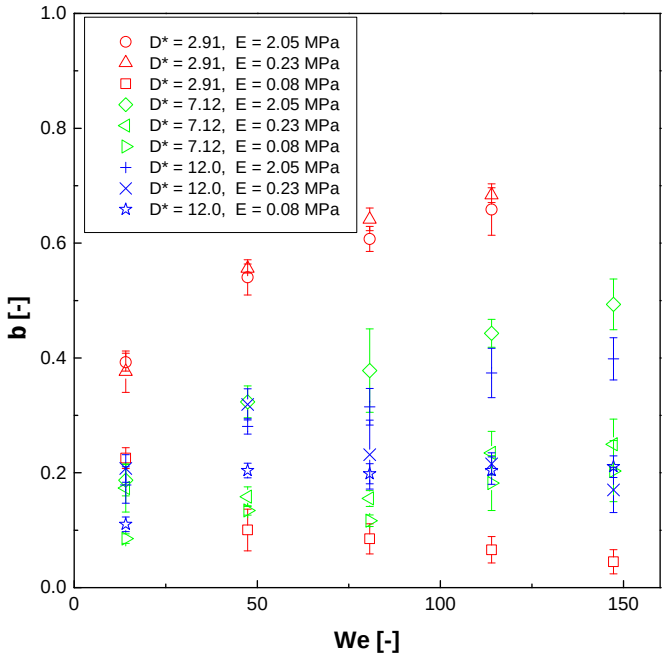


FIG. 13: Retraction coefficient as a function of impact Weber number for cases of different diameter ratios and elastic moduli.

Especially in the case of the lowest diameter ratio (red symbols), the minimum length of the wetted arc for substrates with high/intermediate stiffness (E=2.05 MPa or E=0.23 MPa) remains around 1 regardless of the increase of Weber number. The data for Weber number ~147 are unavailable since the flow instabilities at high impact velocity lead to symmetry break during the retraction of the drop, and the drop partially or completely slide off the top of the hemispherical substrate (see case **C (3)** in Figure 10 for example). However the minimum length of the wetted arc for the case of most soft substrate (E=0.08 MPa) increases significantly as the Weber number grows and is only slightly smaller than the maximum one (compare the red square data between Figure 11 and Figure 12), which means the periphery of the drop almost stays pinned after maximum spreading. In case of higher diameter ratios ($D^*$ = 7.12 & $D^*$ = 12.0), although the data for any substrate stiffness seem to rise with the increase of Weber number, the minimum length of the wetted arc for the highest stiffness substrate (E=2.03 MPa) is systematically lower compared to the other two cases of softer substrates. In order to better characterize the retraction behaviour, a quantity which is referred as the retraction coefficient is defined:

$$\beta = (\alpha_{\max} - \alpha_{\min})/\alpha_{\max}. \quad (3)$$

It expresses the relative decrease in the maximum spreading angle due to retraction with respect to the magnitude of maximum spreading angle. Figure 13 shows the retraction coefficient as a function of impact Weber number

for different impact parameters. In the cases of highest-stiffness substrates (symbols: ○,◇,+), the retraction is more pronounced as the Weber number increases for all diameter ratios, which is reasonable since larger impact velocity will result in higher retraction velocity of the liquid lamella. Surprisingly the data for the smallest diameter ratio (○) are systematically higher than those with larger diameter ratios (◇,+). Here this effect is called the 'de-wetting effect' due to the curvature of the surface, which indicates that impacting drops experience a more significant retraction phase on a substrate with higher curvature. In the case of substrates with intermediate stiffness (△,◁,×), the de-wetting effect is still applicable though some data of highest diameter ratio (×) is comparable or even higher than those with a higher curvature (◁). However the de-wetting effect completely fails in cases of substrates with lowest stiffness (□,▷,☆). The substrate with highest diameter ratio (☆) yields most pronounced retraction. The retraction coefficient of impacting drops on substrate with lowest diameter ratio (□) even decreases with the increase of Weber number, also the values of $\beta$ are below 0.1 when the Weber number is higher than 50, which means the peripheries of spreading drops almost remain stationary after maximum spreading. Thus the effect of diameter ratio on the retraction behaviours in case of the most soft substrate is totally different from the other two cases with a higher-stiffness substrate.

### C. Dynamic contact angle

#### 1. Effect of elastic modulus on dynamic contact angle

The dynamic contact angle as a function of time showing the effect of elastic modulus is displayed in Figure 14 (corresponding to the cases of morphology shown in Figure 8). All the experimental data of dynamic contact angle in this study is measured from the left contact point. The length of the wetted arc is also shown as open symbols in order to provide a clear reference of the impact phases (i.e. spreading, retracting & oscillating). As shown in Figure 14, the dynamic contact angle during spreading and the early stages of retraction is almost consistent for all cases. However, as retraction progresses the softness of the substrate is observed to dampen the dynamic contact angle oscillations (see blue triangle data in **[A]** & **[D]** and green circle data in **[D]**). This is due to contact line pinning after maximum spreading (see the corresponding open symbols for length of the wetted arc). The oscillation amplitude of the dynamic contact angle is considerably reduced for a softer substrate since the contact line is fixed. Nevertheless the effect of the substrate stiffness on the dynamic contact angle is much less significant in cases of smaller curvature (**[B]**) and lower impact Weber number (**[C]**).

#### 2. Effect of diameter ratio on dynamic contact angle

The effect of diameter ratio on the temporal evolution of the dynamic contact angle is shown in Figure 15 (corresponding to the cases of morphology shown in Figure 9). Similar to the effect of substrate stiffness on the dynamic contact angle, the surface curvature does not play an important role during the spreading and early retracting stages. However the increase in the curvature of the surface (i.e. the decrease in the diameter ratio) is observed to enlarge the oscillation amplitude of the dynamic contact angle after the retraction of the drop (see red square data in **[A]** & **[D]**); this is associated with a larger and faster retraction of the contact line (de-wetting). The differences in the de-wetting behavior can be explained in terms of the surface deformation upon impact, which absorbs part of the impact kinetic energy. In the following section (IV A), this mechanism will be discussed in details. Nevertheless the dynamic contact angle is much less affected by the diameter ratio when the stiffness of the substrate is very low (**[B]**, where the pinned effect dominates) or the Weber number is small (**[C]**).

#### 3. Effect of Weber number on dynamic contact angle

The dynamic contact angle as a function of impact time for different Weber numbers is shown in Figure 16 (corresponding to the cases of morphology shown in Figure 10). The increase in the impact Weber number is observed to systematically reduce the dynamic contact angle in all cases. In addition, the oscillation of the dynamic contact angle after drop retraction is significantly inhibited when the Weber number increases to 147 (see filled blue triangle data in Figure16). However if the Weber number is sufficiently low (see red square data in Figure16), a pronounced oscillation phase with large oscillation amplitude of the dynamic contact angle is observed regardless of the diameter ratio or the elastic modulus of the substrate.

## IV. DISCUSSION

### A. Energy dissipation due to substrate deformation

In this section, the influence of the diameter ratio and of the elastic modulus on the spreading behavior is interpreted in the light of the substrate deformation energy. Firstly, a simple scenario, schematically shown in Figure 17 (A) is considered, where a drop impacts on a flat elastic surface and reaches the maximum spreading diameter. The surface is deformed (as indicated by the dashed line) due to the pressure exerted by the impacting drop. Since an element of surface which is closer to the impact center experiences a longer contact time during impact, the magnitude of deformation, $\delta y(r)$ reaches its maximum ($\delta y_{\max}$) at the center of impact, and decreases radially

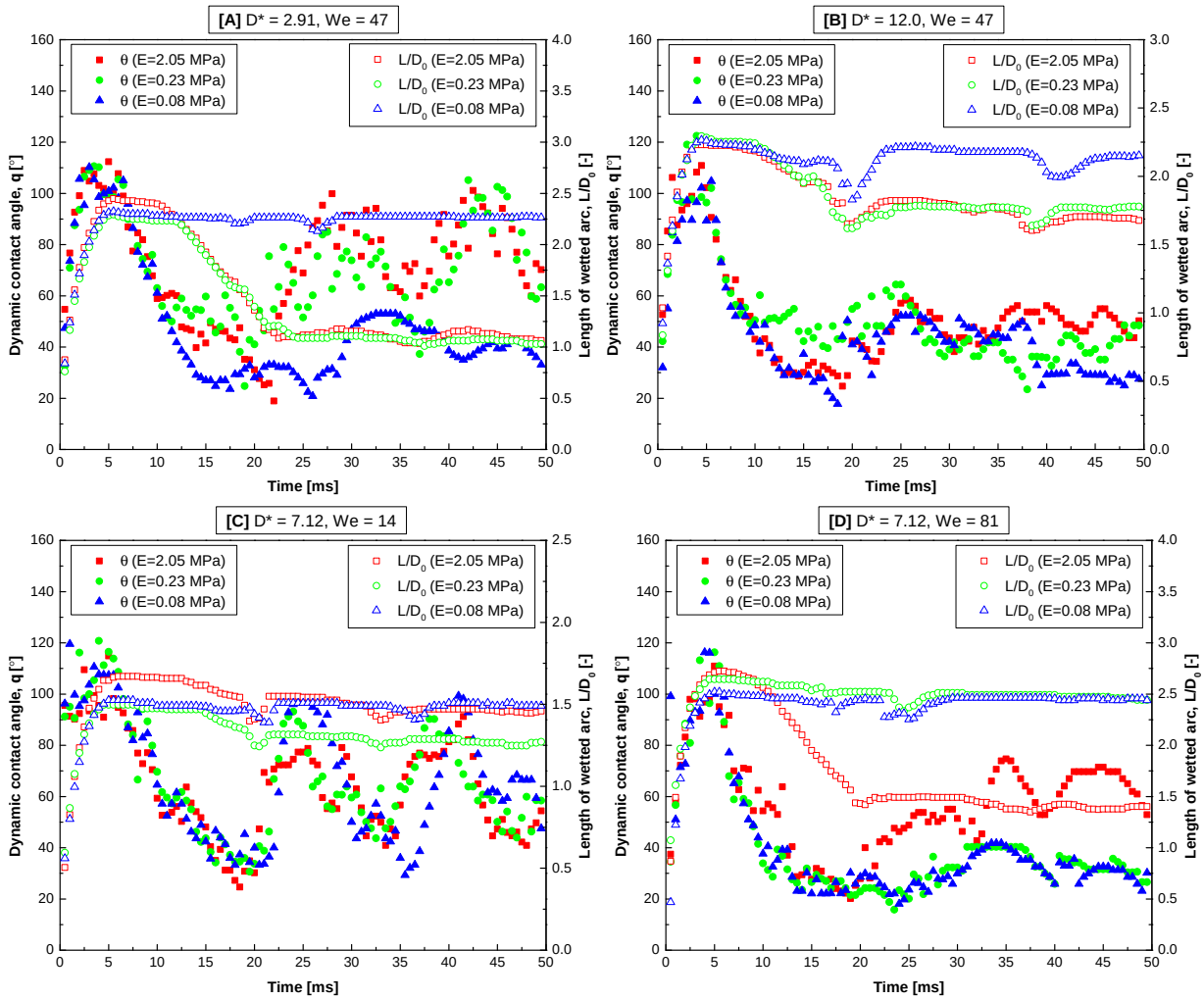


FIG. 14: Dynamic contact angle as a function of impact time showing the effect of elastic modulus. The impact parameters in each subfigure (A, B, C & D) correspond to the image sequence group (A, B, C & D) in Figure 8. Filled symbols represent the data of dynamic contact angle while the length of wetted arc is denoted by open symbols.

with the distance from the center, $r$, up to a value of zero at maximum spreading radius, $r_{\max}$. To simplify the quantitative estimate of the elastic energy stored by the substrate, the contour of the deformed surface is approximated by a parabola:

$$\delta y(r) = \delta y_{\max}[1 - (\frac{r}{r_{\max}})^2]. \tag{4}$$

Let $P_{\text{ave}}$ represent the average pressure subjected by the surface with respect to spreading time; then, the normal force on an infinitely small annular surface area can be written as:

$$\mathrm{d}F = P_{\text{ave}} \cdot 2\pi r \mathrm{d}r, \tag{5}$$

and the corresponding differential expression of deformation energy is given by:

$$\mathrm{d}W_{\text{def}} = \mathrm{d}F \cdot \delta y = 2\pi P_{\text{ave}} \delta y_{\max}[1 - (\frac{r}{r_{\max}})^2] r \mathrm{d}r. \tag{6}$$

Thus the total deformation energy during impact can be obtained by the integral of Equation 6 with respect to $r$:

$$\begin{aligned} W_{\text{def}} &= \int_0^{r_{\max}} \mathrm{d}W_{\text{def}} \\ &= 2\pi P_{\text{ave}} \delta y_{\max} \int_0^{r_{\max}} [1 - (\frac{r}{r_{\max}})^2] r \mathrm{d}r \\ &= \frac{1}{2}\pi P_{\text{ave}} \delta y_{\max} r_{\max}^2 \ (= \frac{1}{8}\pi P_{\text{ave}} \delta y_{\max} L_{\max}^2). \end{aligned} \tag{7}$$

Secondly, this simplified model is extended to the case of a spherical elastic surface (Figure 17 (B)). If the impact kinetic energy is the same, i.e. the impacting drops have the same Weber number, one can expect the vertical pressure ($P_{\text{ave}}$) on the impact surface to be almost identical for two cases. However, in the case of a spherical surface, only the normal component of $P_{\text{ave}}$ to the target surface is responsible for its deformation, while the tangential component contributes to spreading. As a

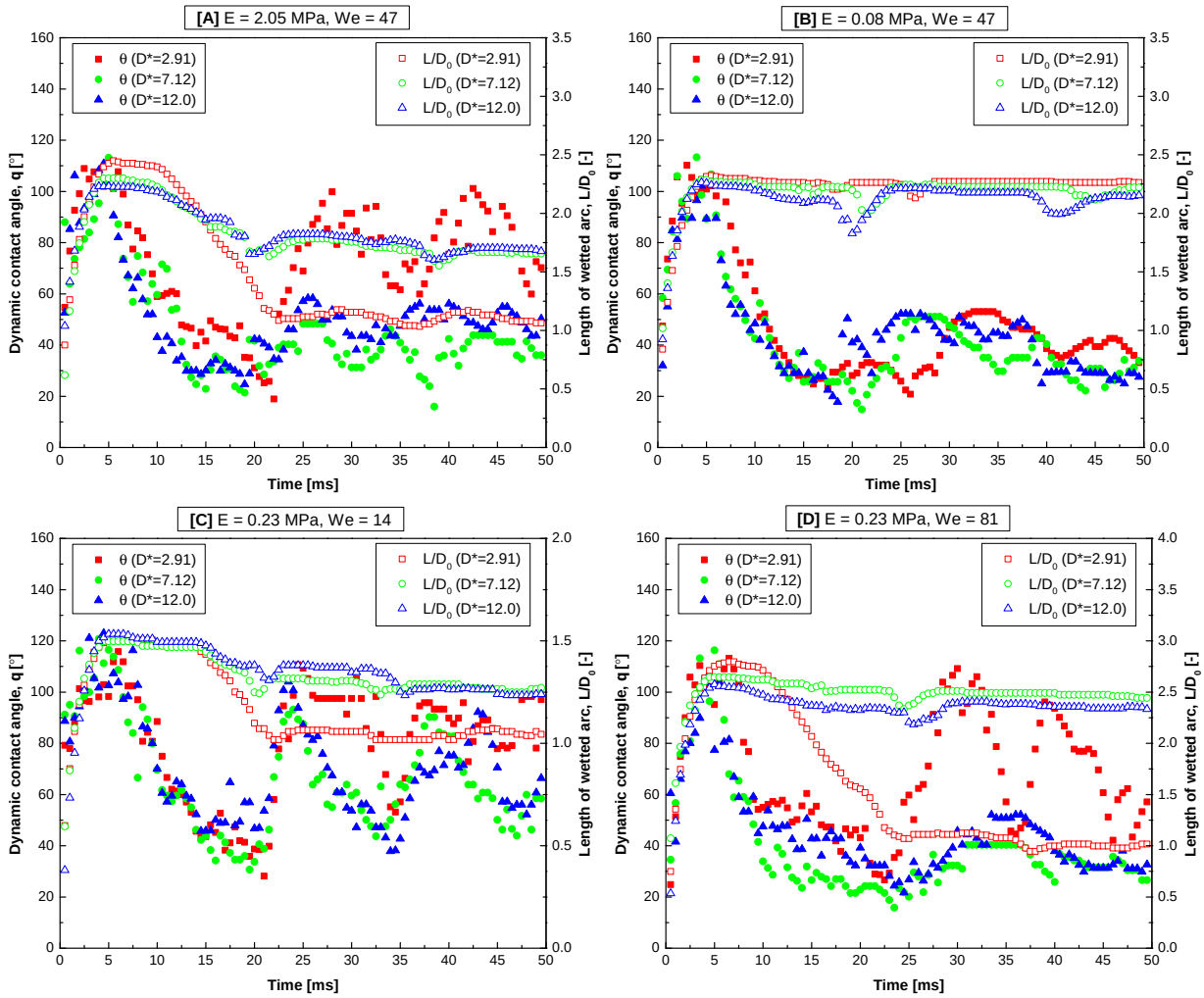


FIG. 15: Dynamic contact angle as a function of time for different diameter ratios. The impact parameters in each subfigure (A, B, C & D) correspond to the image sequence group (A, B, C & D) in Figure 9.

result, the differential expression of normal force on the substrate surface shown by Equation 5 can be modified for the case of a spherical surface as:

$$\begin{aligned} \mathrm{d}F^* &= P_{\mathrm{ave}} \cos\omega \cdot 2\pi R_{sub}^2 \sin\omega \mathrm{d}\omega \\ &= \pi P_{\mathrm{ave}} R_{sub}^2 \sin 2\omega \mathrm{d}\omega, \end{aligned} \tag{8}$$

where $\omega$ is the polar coordinate measured form the center of the spherical substrate, and $R_{sub}$ denotes the radius of the substrate. Similar to Equation 4, a parabolic deformed contour is assumed to radially distribute on the target surface:

$$\delta y^*(\omega) = \delta y_{\max}[1 - (\frac{\omega}{\omega_{\max}})^2], \ (\omega_{\max} = \frac{L_{\max}}{2R_{sub}}). \tag{9}$$

By integrating the product of Equation 8 and Equation 9 with respect to $\omega$, the total deformation energy for the case of a spherical surface can be expressed as:

$$\begin{aligned} W_{\mathrm{def}}^* &= \int_0^{\omega_{\max}} \mathrm{d}W_{\mathrm{def}}^* \\ &= \int_0^{\omega_{\max}} \mathrm{d}F^* \delta y^*(\omega) \\ &= \pi P_{\mathrm{ave}} R_{sub}^2 \delta y_{\max} \\ &\quad \times \int_0^{\omega_{\max}} [1 - (\frac{\omega}{\omega_{\max}})^2] \sin 2\omega \mathrm{d}\omega \\ &= \pi P_{\mathrm{ave}} R_{sub}^2 \delta y_{\max} \\ &\quad \times (\frac{1}{2} + \frac{\sin^2 \omega_{\max} - \omega_{\max} \sin 2\omega_{\max}}{2\omega_{\max}^2}) \end{aligned} \tag{10}$$

Substituting $R_{sub} = D^* D_0/2$ and $\omega_{\max} = L_{\max}/2R_{sub} = L_{\max}/(D^* D_0)$ into Equation 10, the deformation energy

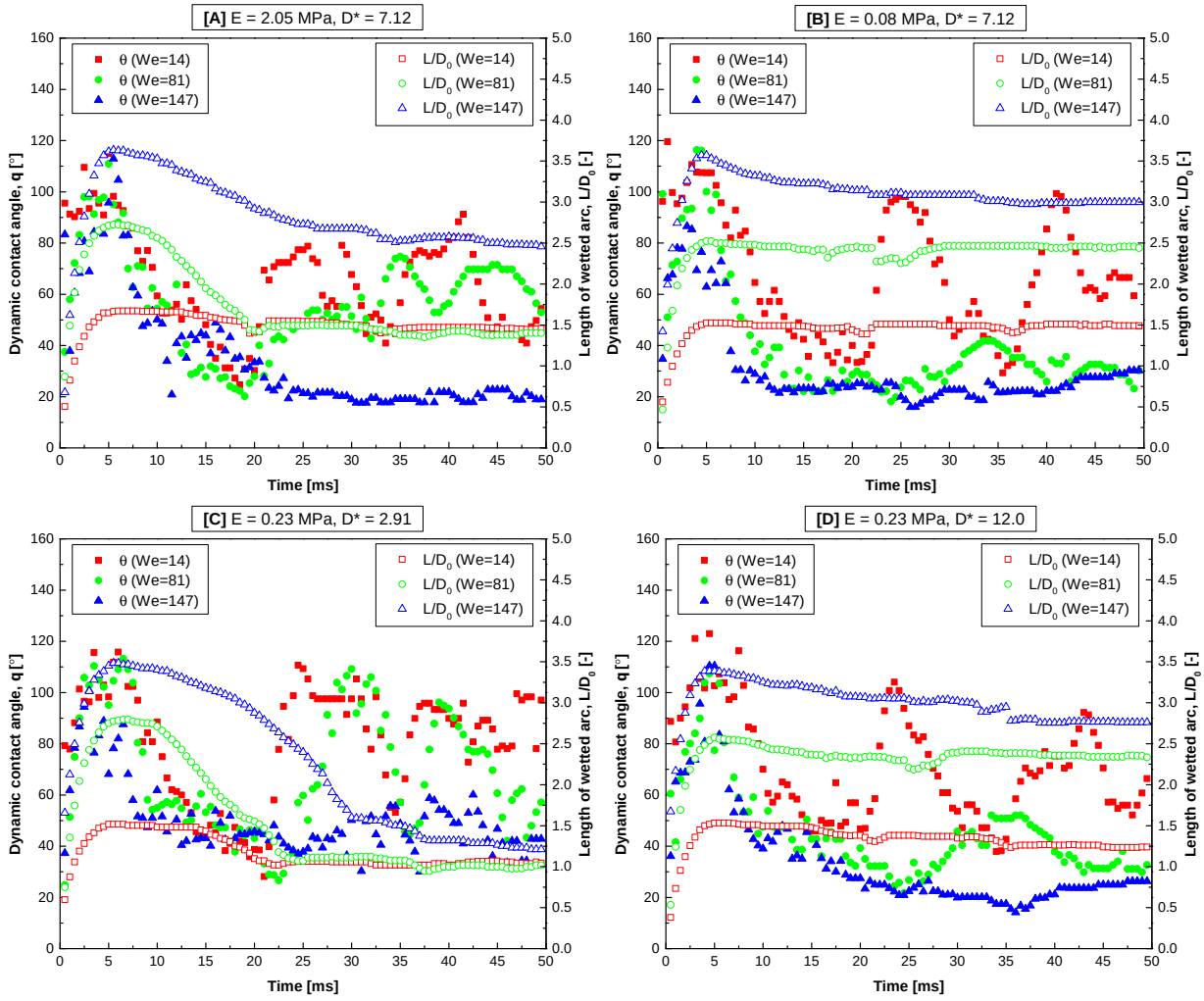


FIG. 16: Dynamic contact angle as a function of time for different Weber numbers. The impact parameters in each subfigure (A, B, C & D) correspond to the image sequence group (A, B, C & D) in Figure 10.

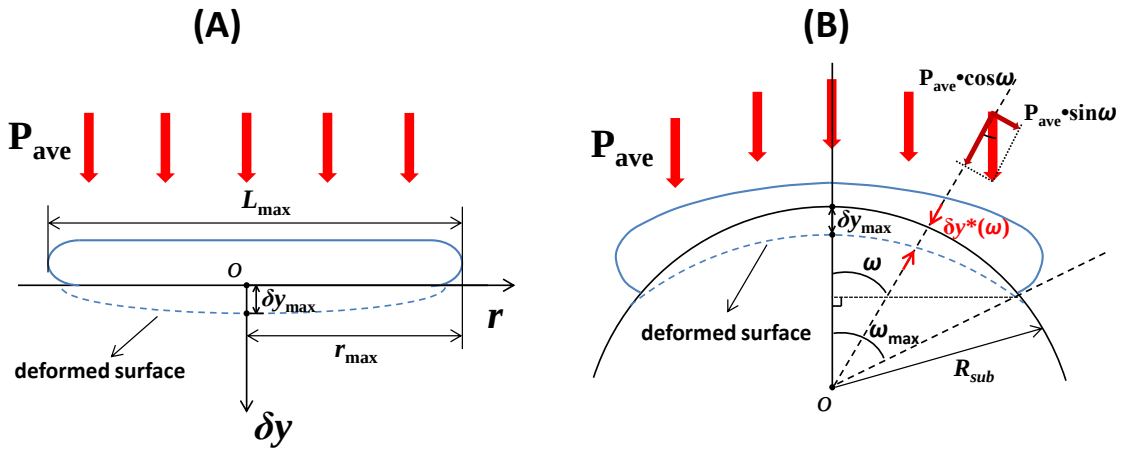


FIG. 17: Schematic of energy dissipation mechanism due to substrate deformation: (A) drop impact on flat elastic substrate; (B) drop impact on spherical elastic substrate.

as a function of $D^*$ is obtained:

$$W^*_{\rm def} = \frac{\pi P_{\rm ave}\delta y_{\rm max}(D^*D_0)^4}{8L^2_{\rm max}} \times [\frac{L_{\rm max}}{D^*D_0}(\frac{L_{\rm max}}{D^*D_0} - \sin\frac{2L_{\rm max}}{D^*D_0}) + \sin^2\frac{L_{\rm max}}{D^*D_0}]. \quad (11)$$

Let $\overline{L}_{\rm max} = L_{\rm max}/D_0$ denote the normalized maximum length of the wetted arc, then Equation 11 can be simplified as:

$$\begin{aligned} W^*_{\rm def} &= \frac{\pi P_{\rm ave}\delta y_{\rm max}D_0^2(D^*)^4}{8\overline{L}^2_{\rm max}} \times [\frac{\overline{L}_{\rm max}}{D^*}(\frac{\overline{L}_{\rm max}}{D^*} - \sin\frac{2\overline{L}_{\rm max}}{D^*}) + \sin^2\frac{\overline{L}_{\rm max}}{D^*}] \quad (12)\\ &= \frac{\pi P_{\rm ave}\delta y_{\rm max}D_0^2}{8}\cdot\Phi(D^*,\overline{L}_{\rm max}) \end{aligned}$$

where

$$\Phi(D^*,\overline{L}_{\rm max}) = \frac{(D^*)^4}{\overline{L}^2_{\rm max}}[\frac{\overline{L}_{\rm max}}{D^*}(\frac{\overline{L}_{\rm max}}{D^*} - \sin\frac{2\overline{L}_{\rm max}}{D^*}) + \sin^2\frac{\overline{L}_{\rm max}}{D^*}]. \quad (13)$$

According to the impulse-momentum theorem, the momentum change ($m\Delta u_y$) of the drop in the vertical direction during impact is equal to the average force ($F$) applied on the drop times its duration ($\Delta t$):

$$\begin{aligned} F\Delta t &= P_{\rm ave}\pi(R_{sub}\sin\omega_{\rm max})^2\Delta t\\ &= \frac{\pi P_{\rm ave}(D_0D^*\sin\frac{\overline{L}_{\rm max}}{D^*})^2}{4}\Delta t = m\Delta u_y, \end{aligned} \quad (14)$$

where $\Delta u_y = u_i - 0 = u_i$ because the vertical velocity of the drop decreases from the impact velocity ($u_i$) to zero during impact, and the impact duration can be approximated by the characteristic time:

$$\Delta t \approx \frac{D_0}{u_i}. \quad (15)$$

Thus the average pressure can be estimated as:

$$P_{\rm ave} \approx \frac{4mu_i^2}{\pi D_0^3(D^*\sin\frac{\overline{L}_{\rm max}}{D^*})^2} \quad (16)$$

In order to estimate the magnitude of $\delta y_{\rm max}$, the classical solution for elastic contact mechanics between two spheres is adopted to correlate the force and the maximum deformation[50]:

$$F = \frac{4}{3}\cdot\frac{E}{1-\nu^2}\cdot R_{\rm eff}^{\frac{1}{2}}\delta y_{\rm max}^{\frac{3}{2}} \approx \frac{4}{3}\cdot ER_{\rm eff}^{\frac{1}{2}}\delta y_{\rm max}^{\frac{3}{2}}, \quad (17)$$

where $\nu$ is the Poisson's ratio, $F$ (Equation 14) is the applied force, and $R_{\rm eff}$ represents the effective radius:

$$R_{\rm eff} = \frac{R_1R_2}{R_1+R_2} = \frac{D^*D_0}{2(1+D^*)}, \quad (18)$$

in which $R_1$ and $R_2$ denote the radii of the two spheres. Thus, from Equations 17 & 18 $\delta y_{\rm max}$ is estimated as:

$$\delta y_{\rm max} = \frac{u_i}{2D_0D^*\sin\frac{\overline{L}_{\rm max}}{D^*}}\sqrt[3]{\frac{9(1+D^*)m^2u_i}{D^*E^2}} \quad (19)$$

Combing Equations 12, 16 & 19, the deformation energy for the case of a spherical substrate can be rewritten as:

$$W^*_{\rm def} = \frac{\sqrt[3]{9}m^{\frac{5}{3}}u_i^{\frac{10}{3}}}{4(D_0D^*\sin\frac{\overline{L}_{\rm max}}{D^*})^2E^{\frac{2}{3}}}\sqrt[3]{\frac{1+D*}{D*}}\cdot\Phi(D^*,\overline{L}_{\rm max}) \quad (20)$$

Substituting the drop mass, $m = (1/6)\pi\rho D_0^3$ into Equation 20, $W^*_{\rm def}$ can be rewritten as:

$$W^*_{\rm def} = \frac{\frac{1}{3}(\frac{1}{2})^{\frac{11}{3}}(\pi\sigma We)^{\frac{5}{3}}D_0^{\frac{4}{3}}}{(D^*\sin\frac{\overline{L}_{\rm max}}{D^*})^2E^{\frac{2}{3}}}\sqrt[3]{\frac{1+D*}{D*}}\cdot\Phi(D^*,\overline{L}_{\rm max}), \quad (21)$$

where $We = \rho u_i^2D_0/\sigma$ is the Weber number.

### B. Considerations on the energy balance

A simple energy balance approach[51–53] can be used to estimate the maximum length of the wetted arc reached by a water droplet impacting on an elastic spherical substrate. Whilst energy (or momentum) conservation approaches are very popular due to their simplicity, it must be kept in mind their accuracy relies heavily on empirical coefficients. In particular, it is well-known that if the fluid viscosity is not close to that of water, all drop impact models based on energy conservation fail to predict experimental results with an acceptable error[6]; it was also shown that if the model coefficients are judiciously adjusted the scaling $D_{max}/D_0 \sim We^{1/2}$ can fit experimental data in a very large range of the variables[54]. In other words, if one locks the Weber number exponent and shifts all the empirical input on the other coefficients, it is still possible to obtain very good agreement with experiments, but this does not mean the scaling is true.

Equating the kinetic energy ($E_{\rm k}^{(b)}$) and surface energy ($E_{\rm s}^{(b)}$) of a spherical drop before impact to the sum of the kinetic energy (which is assumed to be zero), surface energy ($E_{\rm s}^{(m)}$), viscous dissipation energy ($W_{\rm vis}$) and energy dissipation due to substrate deformation ($W^*_{\rm def}$) at maximum spreading, the energy balance yields:

$$E_{\rm k}^{(b)} + E_{\rm s}^{(b)} = E_{\rm s}^{(m)} + W_{\rm vis} + W^*_{\rm def}. \quad (22)$$

The kinetic energy before impact is simply written as:

$$E_{\rm k}^{(b)} = \frac{1}{2}mu_i^2 = \frac{1}{12}\pi\rho D_0^3u_i^2 = \frac{1}{12}\pi\sigma D_0^2We, \quad (23)$$

and the surface energy of a spherical drop is:

$$E_{\rm s}^{(b)} = \pi D_0^2\sigma. \quad (24)$$

The drop shape at maximum spreading is assumed to be a spherical cap with a bottom surface area of $A_b = 2\pi R_{sub}^2(1-\cos\omega_{\max})$, a thickness of $T_c = (1/6\pi D_0^3)/A_b$, and a rim area of $A_r = 2\pi R_{sub}\sin\omega_{\max}\cdot T_c$. The surface energy at maximum spreading is the sum of surface energy at the liquid-gas interface $E_{\mathrm{s,LG}}^{(m)}$, and the surface energy at the liquid-solid interface $E_{\mathrm{s,LS}}^{(m)}$, minus the surface energy at the solid-gas interface $E_{\mathrm{s,SG}}^{(m)}$, which is gradually lost during the impact process:

$$\begin{aligned} E_{\mathrm{s}}^{(m)} &= E_{\mathrm{s,LG}}^{(m)} + E_{\mathrm{s,LS}}^{(m)} - E_{\mathrm{s,SG}}^{(m)} \\ &= (A_b + A_r)\sigma_{LG} + A_b\sigma_{LS} - A_b\sigma_{SG}, \end{aligned} \tag{25}$$

where $\sigma_{LG}$ is the liquid-gas surface tension, $\sigma_{LS}$ is the liquid-solid surface tension, and $\sigma_{SG}$ is the solid-gas surface tension. According to Young's Equation, the difference between $\sigma_{SG}$ and $\sigma_{LS}$ can be correlated to $\sigma_{LG}$ by the static contact angle $\theta_0$:

$$\sigma_{SG} - \sigma_{LS} = \sigma_{LG}\cos\theta_0. \tag{26}$$

Combining Equations 25 and 26, $E_{\mathrm{s}}^{(m)}$ is written as:

$$\begin{aligned} E_{\mathrm{s}}^{(m)} =& [A_b(1-\cos\theta_0) + A_r]\sigma_{LG} \\ =& \frac{\pi(D^*D_0)^2}{2}(1-\cos\frac{\overline{L}_{\max}}{D^*})(1-\cos\theta_0)\sigma \\ &+ \frac{\pi D_0^2\sin\frac{\overline{L}_{\max}}{D^*}}{3D^*(1-\cos\frac{\overline{L}_{\max}}{D^*})}\sigma, \end{aligned} \tag{27}$$

Using the boundary layer thickness (determined from the analytical solution of an axisymmetric stagnation point flow) as the length scale associated with the viscous dissipation term, Pasandideh-Fard *et al.* derived an expression of the energy lost due to viscous dissipation:

$$W_{\mathrm{vis}} = \frac{\pi}{3}\rho u_i^2 D_0 L_{\max}^2\frac{1}{\sqrt{Re}} = \frac{\pi}{3}\sigma(\overline{L}_{\max}D_0)^2 We Re^{-\frac{1}{2}}, \tag{28}$$

Although Equation 28 was obtained for the case of a flat surface, here it is adopted to estimate the viscous energy dissipation for spherical surfaces as an approximation (in particular, the error decreases as the diameter ratio $D^*$ increases).

Substituting $E_{\mathrm{k}}^{(b)}$, $E_{\mathrm{s}}^{(b)}$, $E_{\mathrm{s}}^{(m)}$, $W_{\mathrm{vis}}$ and $W_{\mathrm{def}}^*$, given by Equations 23, 24, 27, 28 and 21, respectively, into the energy balance equation (Equation 22), a correlation between the Weber number ($We$) and normalised maximum length of the wetted arc ($\overline{L}_{\max}$) can be established. Given a certain value of the Weber number, $\overline{L}_{\max}$ can be obtained by Equation 22 since all the other parameters are known. The normalised maximum length of the wetted arc is plotted in Figure 18 (dash-dot line) as a function of $We$ for a parameter set of $E$ = 0.08 MPa & $D^*$ = 12.0 (i.e., the case where the energy dissipation due to deformation is the highest). The results are compared with different predictions using the same model, and considering: (i) no energy dissipation (solid line); (ii) only the energy dissipation due to substrate deformation (dashed line); (iii) only the viscous energy dissipation (dotted line). The experimental data for the same parameter set and the best fit line (from Figure 11) are also shown for comparison. As shown in Figure 18, taking into account the energy dissipation due to deformation without viscous energy dissipation decreases the predicted values only slightly, while the prediction is closer to experimental data if the viscous dissipation is taken into account, because the viscous energy dissipation in the fluid is much larger than the dissipation due to surface deformation. The model predictions of $\overline{L}_{\max}$ for all the cases reported in Figure 11 are plotted and compared with the corresponding experimental results in Figure 19. The model results confirm the effects of elastic modulus and diameter ratio on the spreading behaviours are modest and do not change the scaling of the maximum spreading length with respect to the Weber number. However, the proposed energy conservation approach is not able to predict the scaling $L_{max}/D_0 \sim We^{0.33}$ observed experimentally.

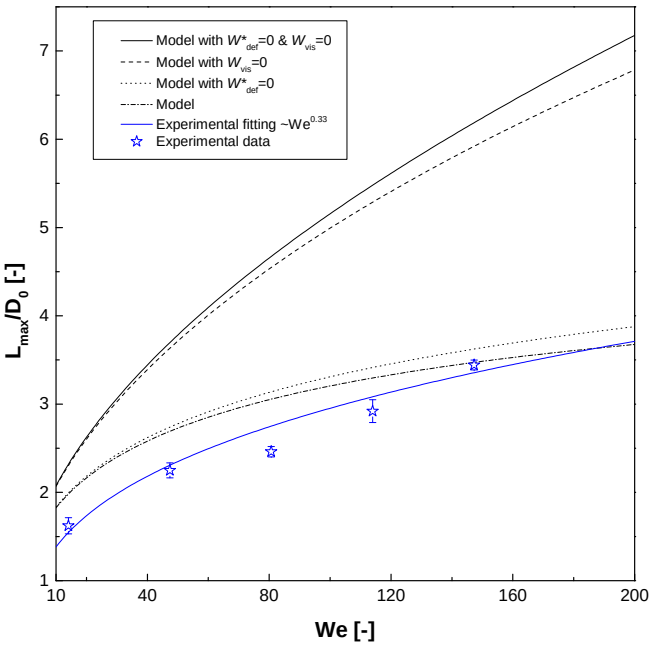


FIG. 18: The normalised maximum length of the wetted arc as a function of Weber number for a parameter set of E = 0.08 MPa & D* = 12.0. Lines of different types represent the model predictions with different energy dissipations: no energy dissipation (solid line); only the dissipation due to deformation (dashed line); only viscous dissipation (dotted line); energy dissipations due to both viscous forces and deformation (dash-dot line). Blue star and line indicate the experimental data and fitting, respectively.

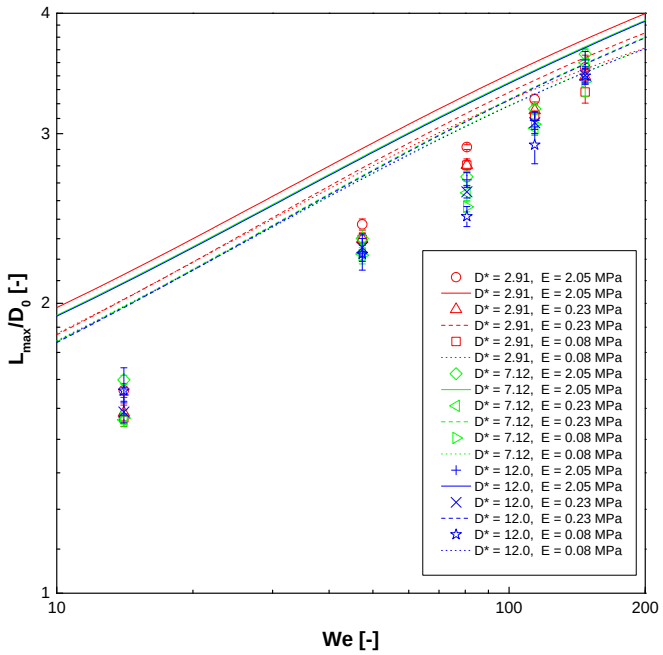


FIG. 19: The normalised maximum length of the wetted arc as a function of impact Weber number for cases of different diameter ratios and elastic moduli. Lines of different types and colors represent the model predictions, and symbols denote the experimental data.

## V. CONCLUSIONS

The impact of water drops on convex, hemispherical, elastic surfaces was investigated experimentally by means of high-speed imaging. Convex hemispherical elastic substrates characterized by different diameters and different elastic moduli were produced using a polydimethylsiloxane (PDMS) silicone elastomer. The impact morphology was characterized through several quantities, including the maximum and the minimum spreading angles, the length of the wetted curve and the dynamic contact angle. In particular, the dynamic contact angle was measured utilizing a novel digital image processing scheme based on a goniometric mask.

The morphology of the impacting drop was studied under different impact parameters. In particular, the effect of three independent impact parameters (elastic modulus, diameter ratio and Weber number) on the dynamic contact angle has been systematically investigated. The decrease in the elastic modulus of the substrate and the increase in the diameter ratio are observed to inhibit the oscillation of the dynamic contact angle after impact at sufficiently high Weber number, where both the deformation energy and the viscous dissipation become significant. However the effect of elastic modulus (or diameter ratio) is much less significant if the diameter ratio is very high (or the elastic modulus is very low). The increase in the impact Weber number is observed to systematically reduce the dynamic contact angle in all combinations of impact parameters.

Results show that the effect of diameter ratio and elastic modulus on spreading behaviours of the drops is limited. The retraction of the drop impacting on the substrate with lowest stiffness is significantly inhibited because of contact line pinning. Drops impacting on a surface with higher curvature (i.e. lower diameter ratio) are observed to experience a more pronounced retraction phase compared to the case of a small curvature. A simple energy conservation approach accounting for the energy dissipation due to substrate deformation can expain some of the experimental observations, however is not able to predict the scaling of the maximum spreading length without further empirical adjustments.

## ACKNOWLEDGMENTS

S. Chen gratefully acknowledges financial support from the China Scholarship Council (CSC).

[1] A. Worthington, "On the forms assumed by drops of liquids falling vertically on a horizontal plate," Proceedings of the royal society of London **25**, 261–272 (1876).
[2] M. Rein, "Phenomena of liquid drop impact on solid and liquid surfaces," Fluid Dynamics Research **12**, 61–93 (1993).
[3] A. Yarin, "Drop impact dynamics: splashing, spreading, receding, bouncing," Annu. Rev. Fluid Mech. **38**, 159–192 (2006).
[4] C. Mundo, M. Sommerfeld, and C. Tropea, "Droplet-wall collisions: experimental studies of the deformation and breakup process," International journal of multiphase flow **21**, 151–173 (1995).
[5] R. Rioboo, M. Marengo, and C. Tropea, "Time evolution of liquid drop impact onto solid, dry surfaces," Experiments in Fluids **33**, 112–124 (2002).
[6] G. German and V. Bertola, "Review of drop impact models and validation with high-viscosity newtonian fluids," Atomization and Sprays **19** (2009).
[7] S. Sampath and X. Jiang, "Splat formation and microstructure development during plasma spraying: deposition temperature effects," Materials Science and Engineering: A **304**, 144–150 (2001).
[8] J. Field, J. Dear, and J. Ogren, "The effects of target compliance on liquid drop impact," Journal of Applied Physics **65**, 533–540 (1989).
[9] C. Extrand and Y. Kumagai, "Contact angles and hysteresis on soft surfaces," Journal of colloid and interface science **184**, 191–200 (1996).
[10] R. Pericet-Cámara, A. Best, H.-J. Butt, and E. Bonaccurso, "Effect of capillary pressure and surface tension on the deformation of elastic surfaces by sessile liquid microdrops: an experimental investigation," Langmuir **24**, 10565–10568 (2008).
[11] R. Pericet-Camara, G. K. Auernhammer, K. Koynov, S. Lorenzoni, R. Raiteri, and E. Bonaccurso, "Solid-supported thin elastomer films deformed by microdrops," Soft Matter **5**, 3611–3617 (2009).
[12] E. R. Jerison, Y. Xu, L. A. Wilen, and E. R. Dufresne, "Deformation of an elastic substrate by a three-phase contact line," Physical review letters **106**, 186103 (2011).
[13] R. W. Style and E. R. Dufresne, "Static wetting on deformable substrates, from liquids to soft solids," Soft Matter **8**, 7177–7184 (2012).
[14] L. Chen, E. Bonaccurso, and M. E. Shanahan, "Inertial to viscoelastic transition in early drop spreading on soft surfaces," Langmuir **29**, 1893–1898 (2013).

[15]S. Mangili, C. Antonini, M. Marengo, and A. Amirfazli, "Understanding the drop impact phenomenon on soft pdms substrates," Soft Matter **8**, 10045–10054 (2012).
[16]A. Alizadeh, V. Bahadur, W. Shang, Y. Zhu, D. Buckley, A. Dhinojwala, and M. Sohal, "Influence of substrate elasticity on droplet impact dynamics," Langmuir **29**, 4520–4524 (2013).
[17]L. Chen, J. Wu, Z. Li, and S. Yao, "Evolution of entrapped air under bouncing droplets on viscoelastic surfaces," Colloids and Surfaces A: Physicochemical and Engineering Aspects **384**, 726–732 (2011).
[18]R. E. Pepper, L. Courbin, and H. A. Stone, "Splashing on elastic membranes: The importance of early-time dynamics," Physics of Fluids **20**, 082103 (2008).
[19]C. J. Howland, A. Antkowiak, J. R. Castrejón-Pita, S. D. Howison, J. M. Oliver, R. W. Style, and A. A. Castrejón-Pita, "Its harder to splash on soft solids," Physical review letters **117**, 184502 (2016).
[20]T. Vasileiou, J. Gerber, J. Prautzsch, T. M. Schutzius, and D. Poulikakos, "Superhydrophobicity enhancement through substrate flexibility," Proceedings of the National Academy of Sciences , 201611631 (2016).
[21]P. B. Weisensee, J. Tian, N. Miljkovic, and W. P. King, "Water droplet impact on elastic superhydrophobic surfaces," Scientific Reports **6**, 30328 (2016).
[22]S. Gart, J. E. Mates, C. M. Megaridis, and S. Jung, "Droplet impacting a cantilever: A leaf-raindrop system," Physical Review Applied **3**, 044019 (2015).
[23]T. Kajiya, A. Daerr, T. Narita, L. Royon, F. Lequeux, and L. Limat, "Dynamics of the contact line in wetting and diffusing processes of water droplets on hydrogel (pamps-paam) substrates," Soft Matter **7**, 11425–11432 (2011).
[24]S. Chen and V. Bertola, "Morphology of viscoplastic drop impact on viscoplastic surfaces," Soft Matter **13**, 711–719 (2017).
[25]T.-M. Liou, C.-Y. Chan, and K.-C. Shih, "Study of the characteristics of polymer droplet deposition in fabricated rectangular microcavities," Journal of Micromechanics and Microengineering **19**, 065028 (2009).
[26]Y. Hardalupas, A. Taylor, and J. Wilkins, "Experimental investigation of sub-millimetre droplet impingement on to spherical surfaces," International journal of heat and fluid flow **20**, 477–485 (1999).
[27]S. Bakshi, I. V. Roisman, and C. Tropea, "Investigations on the impact of a drop onto a small spherical target," Physics of Fluids **19**, 032102 (2007).
[28]G. Liang, Y. Guo, X. Mu, and S. Shen, "Experimental investigation of a drop impacting on wetted spheres," Experimental Thermal and Fluid Science **55**, 150–157 (2014).
[29]D. Zhang, K. Papadikis, and S. Gu, "Application of a high density ratio lattice-boltzmann model for the droplet impingement on flat and spherical surfaces," International Journal of Thermal Sciences **84**, 75–85 (2014).
[30]D. Zhang, K. Papadikis, and S. Gu, "Investigations on the droplet impact onto a spherical surface with a high density ratio multi-relaxation time lattice-boltzmann model," Communications in Computational Physics **16**, 892–912 (2014).
[31]I. Malgarinos, N. Nikolopoulos, and M. Gavaises, "A numerical study on droplet-particle collision dynamics," International Journal of Heat and Fluid Flow **61**, 499–509 (2016).
[32]M. Pasandideh-Fard, M. Bussmann, and S. Chandra, "Simulating droplet impact on a substrate of arbitrary shape," Atomization and sprays **11** (2001).
[33]G. Liang, Y. Guo, Y. Yang, S. Guo, and S. Shen, "Special phenomena from a single liquid drop impact on wetted cylindrical surfaces," Experimental Thermal and Fluid Science **51**, 18–27 (2013).
[34]G. Liang, Y. Yang, Y. Guo, N. Zhen, and S. Shen, "Rebound and spreading during a drop impact on wetted cylinders," Experimental Thermal and Fluid Science **52**, 97–103 (2014).
[35]H. J. Subramani, T. Al-Housseiny, A. U. Chen, M. Li, and O. A. Basaran, "Dynamics of drop impact on a rectangular slot," Industrial & Engineering Chemistry Research **46**, 6105–6112 (2007).
[36]D. Biolè and V. Bertola, "A goniometric mask to measure contact angles from digital images of liquid drops," Colloids and Surfaces A: Physicochemical and Engineering Aspects **467**, 149–156 (2015).
[37]D. Biolè and V. Bertola, "The fuzzy interface of a drop," Computing and Visualization in Science **17**, 19–32 (2015).
[38]D. Biolè, M. Wang, and V. Bertola, "Assessment of image processing methods to measure the apparent contact angle of liquid drops," Experimental Thermal and Fluid Science **76**, 296–305 (2016).
[39]Y. Rotenberg, L. Boruvka, and A. Neumann, "Determination of surface tension and contact angle from the shapes of axisymmetric fluid interfaces," Journal of colloid and interface science **93**, 169–183 (1983).
[40]O. Del Rıo and A. Neumann, "Axisymmetric drop shape analysis: computational methods for the measurement of interfacial properties from the shape and dimensions of pendant and sessile drops," Journal of colloid and interface science **196**, 136–147 (1997).
[41]M. Hoorfar and A. Neumann, "Recent progress in axisymmetric drop shape analysis (adsa)," Advances in colloid and interface science **121**, 25–49 (2006).
[42]F. Carrillo, S. Gupta, M. Balooch, S. J. Marshall, G. W. Marshall, L. Pruitt, and C. M. Puttlitz, "Nanoindentation of polydimethylsiloxane elastomers: Effect of crosslinking, work of adhesion, and fluid environment on elastic modulus," Journal of materials research **20**, 2820–2830 (2005).
[43]E. A. Wilder, S. Guo, S. Lin-Gibson, M. J. Fasolka, and C. M. Stafford, "Measuring the modulus of soft polymer networks via a buckling-based metrology," Macromolecules **39**, 4138–4143 (2006).
[44]C. M. Cesa, N. Kirchgeßner, D. Mayer, U. S. Schwarz, B. Hoffmann, and R. Merkel, "Micropatterned silicone elastomer substrates for high resolution analysis of cellular force patterns," Review of scientific instruments **78**, 034301 (2007).
[45]D. Fuard, T. Tzvetkova-Chevolleau, S. Decossas, P. Tracqui, and P. Schiavone, "Optimization of poly-di-methyl-siloxane (pdms) substrates for studying cellular adhesion and motility," Microelectronic Engineering **85**, 1289–1293 (2008).
[46]Z. Wang, A. A. Volinsky, and N. D. Gallant, "Crosslinking effect on polydimethylsiloxane elastic modulus measured by custom-built compression instrument," Journal of Applied Polymer Science **131** (2014).
[47]G. German and V. Bertola, "Impact of shear-thinning and yield-stress drops on solid substrates," Journal of Physics: Condensed Matter **21**, 375111 (2009).
[48]S. Chen and V. Bertola, "The impact of viscoplastic drops on a heated surface in the leidenfrost regime," Soft Matter **12**, 7624–7631 (2016).
[49]A.-L. Biance, F. Chevy, C. Clanet, G. Lagubeau, and D. Quéré, "On the elasticity of an inertial liquid shock," Journal of Fluid Mechanics **554**, 47–66 (2006).
[50]D. A. Hanaor, Y. Gan, and I. Einav, "Contact mechanics of fractal surfaces by spline assisted discretisation," International Journal of Solids and Structures **59**, 121–131 (2015).
[51]S. Chandra and C. Avedisian, "On the collision of a droplet with a solid surface," in *Proceedings of the Royal Society of London A: Mathematical, Physical and Engineering Sciences*, Vol. 432 (The Royal Society, 1991) pp. 13–41.
[52]M. Pasandideh-Fard, Y. Qiao, S. Chandra, and J. Mostaghimi, "Capillary effects during droplet impact on a solid surface," Physics of fluids **8**, 650–659 (1996).
[53]T. Mao, D. Kuhn, and H. Tran, "Spread and rebound of liquid droplets upon impact on flat surfaces," AIChE Journal **43**, 2169–2179 (1997).
[54]V. Bertola, "Effect of polymer concentration on the dynamics of dilute polymer solution drops impacting on heated surfaces in the leidenfrost regime," Experimental Thermal and Fluid Science

**52**, 259–269 (2014).